Peering into the Milky Way by FAST:
I. Exquisite HI structures in the inner Galactic disk from the piggyback line observations of the FAST GPPS survey

Tao Hong[1*], JinLin Han[1,2*], LiGang Hou[1], XuYang Gao[1,2], Chen Wang[1], and Tao Wang[1,2]

[1]*National Astronomical Observatories, Chinese Academy of Sciences, Beijing 100101, China;*
[2]*School of Astronomy, University of Chinese Academy of Sciences, Beijing 100049, China*

Neutral hydrogen (HI) is the fundamental component of the interstellar medium. The Galactic Plane Pulsar Snapshot (GPPS) survey is designed for hunting pulsars by using the Five-hundred-meter Aperture Spherical radio Telescope (FAST) from the visible Galactic plane within $|b| \leq 10°$. The survey observations are conducted with the L-band 19-beam receivers in the frequency range of 1.0-1.5 GHz, and each pointing has an integration time of 5 min. The piggyback spectral data simultaneously recorded during the FAST GPPS survey are great resources for studies on the Galactic HI distribution and ionized gas. We process the piggyback HI data of the FAST GPPS survey in the region of $33° \leq l \leq 55°$ and $|b| \leq 2°$. The rms of the data cube is found to be approximately 40 mK at a velocity resolution of 0.1 km s^{-1}, placing it the most sensitive observations of the Galactic HI by far. The high velocity resolution and high sensitivity of the FAST GPPS HI data enable us to detect weak exquisite HI structures in the interstellar medium. HI absorption line with great details can be obtained against bright continuum sources. The FAST GPPS survey piggyback HI data cube will be released and updated on the web: http://zmtt.bao.ac.cn/MilkyWayFAST/.

interstellar medium, atoms, radio lines, surveys

PACS number(s):   98.38.Gt, 95.30.Ky, 95.80.+p, 95.85.Bh

1   Introduction

Neutral hydrogen (HI) is one of the key components of matters in spiral galaxies. It is widely distributed in the Milky Way. The HI gas is the raw material for star formation and plays an important role in galaxy evolution (see refs. [1, 2] and reference therein). Observing the emission line of the Galactic HI gas can reveal the structure and dynamics of the Galaxy over a much extended region in the Galactic disk even in the very far side of the Galaxy. Furthermore, observing the Galactic HI gas is necessary for understanding the life cycles in the Galactic interstellar medium (ISM [3]).

Both single dish radio telescopes and interferometers have been used to observe the Galactic HI gas (see Table 1 [4-13]). Interferometric HI observations [6, 7] can have a high spatial resolution but with a relatively low sensitivity. The VLA Galactic Plane Survey (VGPS [4]) is one of the best rep-

*Corresponding authors (Tao Hong, email: hongtao@nao.cas.cn; JinLin Han, email: hjl@nao.cas.cn)

Table 1   Basic parameters of famous Galactic HI surveys

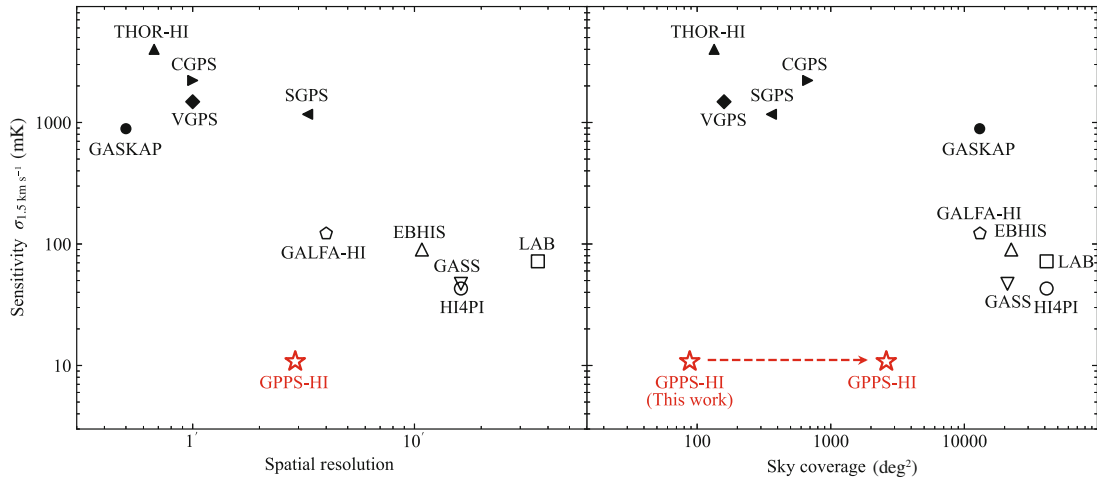| Survey name	Ref.	Sky coverage	Spatial resolution	Velocity range (km s^{-1})	Velocity resolution (km s^{-1})	Sensitivity (mk)
Interferometer surveys						
VGPS	[4]	$18° < l < 67°$ $\|b\| < 1.3°$ to $2.3°$	$1'$	$(-113, +166)$	0.82	2000
GASKAP-HI	[5]	$167 \leq l \leq 79°, \|b\| < 10°$; +Magellanic Stream and Clouds	$30''$	$(-268, +335)$	0.98	1100
CGPS	[6]	$74.2° < l < 147.3°$ $-3.6° < b < 5.6°$	$1'$	$(-165, +60)$	0.82	3000
SGPS	[7]	$5° < l < 20°, 253° < l < 358°$ $\|b\| < 1.5°$	$\sim 3.3'$	$(-227, +265)$	0.8	1600
THOR-HI	[8]	$14.0° < l < 67.4°$ $\|b\| < 1.25°$	$40''$	$(-139, +139)$	1.5	4000
Single dish telescope surveys						
LAB	[9]	full sky	$36'$	$(-400, +400)$	1.25	80
EBHIS	[10]	$\delta \geq -5°$	$10.8'$	$(-600, +600)$	1.44	90
GASS	[11]	$\delta \leq 1°$	$16.2'$	$(-470, +470)$	1.00	57
HI4PI	[12]	full sky	$16.2'$	$(-600, +600)$	1.49	43
GALFA-HI	[13]	$-1° \leq \delta \leq 38°$	$4'$	$(-650, +650)$	0.18	352
GPPS-HI	this work	$\sim 30° < l < \sim 97°, \sim 145° < l < \sim 215°$ $\|b\| \leq 10°$	**2.9$'$**	$(-300, +300)$	**0.10**	**40**

resentatives. It has a high angular resolution of ∼1′ with a sensitivity of 2 K per 0.824 km s^{-1} channel. The ongoing Galactic ASKAP Survey (GASKAP [5,14,15]) improves the spatial resolution to 30″ with a rms noise of 1.1 K per 0.98 km s^{-1}. Single-dish Galactic HI surveys have a much higher sensitivity and cover a much wider region in the sky. One of the most widely-used single-dish Galactic HI surveys is the Leiden/Argentine/Bonn Survey (LAB [9]). This survey was conducted by several 25-m class telescopes, and provides a sensitivity of 80 mK per 1.25 km s^{-1} channel with a coarser spatial resolution of 36′. With multi-beam receivers, the survey efficiency is largely improved, and several modern HI surveys have been accomplished in recent years. Using the 100-m Effelsberg telescope with a seven-beam 1.4-GHz (L-band) receiver, the Effelsberg-Bonn HI Survey (EBHIS [10]) observed the entire northern hemisphere with a sensitivity of 90 mK per 1.44 km s^{-1} channel. GASS [11, 16, 17] mapped the southern sky with a sensitivity of 57 mK per 1.00 km s^{-1} channel by using the L-band 13-beam receiving system mounted on the Parkes 64-m radio telescope. By combining the data of EBHIS and GASS, the HI4PI [12] covers the full sky with a sensitivity of approximately 43 mK and a velocity resolution of 1.49 km s^{-1}, while the spatial resolution is only 16.2′. The Galactic Arecibo L-Band Feed Array HI (GALFA-HI [13,18]) covers the Arecibo sky with a resolution of 4′ and a rms of 352 mK per 0.18 km s^{-1} channel. As summarized in Figure 1, the interferometric surveys (filled black symbols) have a high spatial resolution but a low flux sensitivity, while the single-dish surveys (open symbols) have a wider sky coverage and a higher sensitivity, but with a lower spatial resolution.

HI is a good tracer of Galactic filaments and spiral arms

[19-21]. By adopting the unsharp masking method, Kalberla et al. [22] studied the local Galactic HI distribution and revealed small-scale HI structures with combined data from GASS and EBHIS. Soler et al. [23] searched for HI filaments in the Galaxy with the Hessian matrix method and found a long HI filament named "Maggie" with a length of 1.2 kpc using the data of the HI/OH/Recombination line survey of the inner Milky Way (THOR-HI [8]), and Soler et al. [24] further applied the method to the HI4PI survey [12] and found a large number of filamentary structures even in the very outer Galaxy. By using the HI data observed by the Five-hundred-meter Aperture Spherical radio Telescope (FAST) together with data from the HI4PI, Li et al. [25] detected an HI filament located behind the Outer Scutum-Centaurus (OSC) arm, which might be the farthest HI filament in the Galaxy.

By observing the spectral line signal against strong continuum sources, the HI 21-cm line is shown as absorption features. The strong background sources could be extragalactic radio sources or strong continuum sources within the Milky Way, such as HII regions or supernova remnants (SNRs). Combining HI absorption observations with observation results from molecular lines, one can estimate kinematic distances of SNRs [26, 27]. The HI self-absorption (HISA) traces the cold neutral medium (CNM) which absorbs HI emission from warmer background gas [28, 29]. HI narrow-line self-absorption (HINSA [30]) is a special case of HISA, which is caused by the cold HI that exists around the molecular clouds. Tang el al. [31] and Liu et al. [32] observed HI toward selected Planck Galactic cold clumps by using FAST and detected HINSA features in 58% and 92% of their samples, respectively.

Figure 1 Comparison of the normalized flux sensitivity $\sigma_{1.5 \text{ km s}^{-1}}$ at the same spectral resolution of 1.5 km s^{-1} for the Galactic HI surveys versus the survey spatial resolution (left panel, the best in the bottom left corner) and the sky coverage (right panel, the best in the bottom right corner). The interferometric surveys are labeled with the filled symbols and the single-dish surveys by open symbols. GASKAP-HI: ref. [5]; THOR-HI: ref. [8]; CGPS: ref. [6]; VGPS: ref. [4]; SGPS: ref. [7]; GALFA-HI: ref. [13]; EBHIS: ref. [10]; GASS: ref. [11]; HI4PI: ref. [12]; LAB: ref. [9]; GPPS-HI: this work.

FAST is by far the largest single-dish radio telescope in the world [33]. It provides the highest sensitivity at L-band for pulsar and spectroscopy observations by using the 19-beam receiver [34]. The Galactic Plane Pulsar Snapshot (GPPS) survey[1] [35] is designed for hunting pulsars in the FAST accessible Galactic plane within $|b| \leq 10°$. During the pulsar survey observations, high resolution spectral data are simultaneously recorded in a piggyback mode using another set of backend, covering the band from 1.0 to 1.5 GHz with 1024 K channels. With an integration time of 5 min for each pointing, the sensitivity of HI observations can reach approximately 40 mK at a velocity resolution of 0.1 km s^{-1}, which is by far the most sensitive Galactic HI observation (see Table 1 and Figure 1).

This series of papers are dedicated to investigate the interstellar medium by FAST. This is the first paper for HI gas. The second paper is on the ionized gas by Hou et al. [36], also coming from the piggyback spectral data from the GPPS survey. A study of the Galactic magnetic fields in a deep interstellar space is presented by Xu et al. [37] in the third paper, using mainly the pulsar Faraday rotation measures observed in the GPPS survey. The identification of two large supernova remnants from the FAST-scanned continuum radio maps is presented by Gao et al. [38] in the fourth paper.

In this paper, we process the piggyback HI data from the FAST GPPS survey, and present the HI map for a sky area of 88 square degrees in the inner Galactic disk. The GPPS survey strategy and the spectral data are briefly introduced in sect. 2. We describe the data processing in sect. 3, and the HI results for the sky area of $33° \leq l \leq 55°$, $|b| \leq 2°$ and some

highlights are presented in sect. 4. We summarize the results in sect. 5.

2 The GPPS survey and piggyback spectra

To hunt pulsars, the FAST GPPS survey [35] observes the Galactic plane using the L-band 19-beam receivers. The observations are carried out with a full gain of the FAST in originally down to 26.4° from the zenith but now extended to 28.5°, within which the FAST has an almost full illumination aperture of 300 m. The snapshot observational mode is developed by Han et al. [35] for doing four pointings of the 19 beams (M01 to M19) for 5 min each, and they successively slew the beams, one after another, with a separation of 3′ in between. The beam size at 1420 MHz is 2.82′ to 2.95′, as the beams at the edges of the 19-beam receiver have a slightly larger beam size and stronger side-lobes (see Table 2 of Jiang et al. [34]). The beam-switch takes less than 20 s each, and four pointings of 19 beams take 20 min, so that in 21 min, a hexagonal sky area of 0.1575 square degree can be fully covered by $4 \times 19 = 76$ beams (see Figure 4 in Han et al. [35]). There is almost no overlap for these 76 beams within the extent of the full width half maximum (FWHM), so that the sky coverage is not Nyquist-sampled in terms of beam size. In total 18438 snapshot covers are expected to be carried out for the entire GPPS survey, and about 1800 covers have been observed so far. The detailed observational method and survey strategy of the GPPS survey can be found in Han et al. [35] and the progress can be found on the GPPS web-page[1].

---

1) see http://zmtt.bao.ac.cn/GPPS/ for survey details, including the sky coverage, beam arrangement and current progress.

The GPPS survey records the spectral data together with the pulsar data simultaneously using a separate spectroscopy backend during observations. The major parameters of the GPPS survey and the H I data are summarized in Table 2.

The FAST L-band 19-beam receivers can receive radio signals in the frequency range of 1000-1500 MHz, and they are channelized into 1024 K channels in the digital backend. The four polarization products XX, YY, XY* and YX* are accumulated for a sampling time of 1 s, and recorded simultaneously during the GPPS survey observations for each beam. To calibrate the receiving system, a reference signal with a temperature amplitude of about 1 K was injected to the system every other second. A few 2-min cal-on and cal-off data-takings are conducted in the beginning or the end or in the middle of an observation session for a given day. The data recorded with calibration on-off signal are very useful to calibrate and convert the data unit to the antenna temperature in Kelvin.

3 Processing piggyback H I data of the FAST GPPS survey

A few steps are needed to process the piggyback H I data of FAST GPPS survey, as described in the following.

3.1 Data preparations

One snapshot observation consists of four 5-min pointings. During the observations, the spectroscopy digital backend records the data consecutively without stops but generates a series of fits files, and each contains 128 one-second samplings. Hence for each beam in the snapshot observation of four pointings, ten fits files are written in the FAST data repository for one snapshot observation, including about

Table 2   Parameters for the FAST GPPS survey and piggyback H I spectra

Parameter	Value
FAST aperture diameter	300 m
Beam size	$\sim 2.9'$
System temperature	~ 23 K
Gain	~ 16 K Jy^{-1}
Integration time per pointing	297 s
Galactic longitude range	$\sim 30° < l <\sim 98°$, $\sim 148° < l <\sim 216°$
Galactic latitude range	$|b| \leq 10°$
Frequency range	1000-1500 MHz
Channel number	1024 K
Frequency resolution	476.8 Hz
Velocity resolution for H I	0.1 km s^{-1}
Sensitivity ($\sigma_{0.1 \text{ km s}^{-1}}$)	40 mK

1252 data samplings.

The first step of the data processing is to cut and then combine the ten spectrum files on the basis of the observation time for four pointings. For each beam, the data recorded during the source switching time are discarded, and finally four spectrum files corresponding to the four pointings in the snapshot are prepared, each associated with one pointing position. For 19 beams with four pointings, one gets 76 files for a snapshot observation.

In principle, every pointing for each beam should have on-source time of exactly 300 s. In practice, data shortage for 1 or 2 s occasionally occurs at the very beginning or the end due to either radio frequency interference (RFI) or other telescope operation restrictions, and the real integration time is always about 297 s.

3.2 Calibration on brightness temperature

As mentioned above, in the observation session of a day, two or three or even four data segments are recorded for two minutes each with calibration signals on-off. The digital difference between the averages for the on and off phases, corresponding to the reference level of 1 K temperature in T_a, gives the scale of the snapshot data that day. We apply the scale to the data to convert the received power into antenna temperature T_a. As described by Jiang et al. [34], the electronic gain of the FAST system fluctuates less than 1% over 3.5 h, the band-pass varies about 4% in 30 min. Our observation sessions typically last less than 3 h, the differences between the scales we obtained at the beginning and the end of an observation session are generally less than 5%. The averaged value of the conversion scales over one observation session is applied to minimize the effects of system fluctuations.

Brightness temperature T_b, however, is more often used in studying the Galactic H I emission. To convert the antenna temperature T_a to the brightness temperature T_b, the main beam efficiency is needed. Through the measurements toward the calibrator 3C 138, Gao et al. [38] obtained the FAST gain and the beam-widths for the FAST L-band 19-beam receivers. The main beam efficiency T_a/T_b is then determined, as shown in their Figure 2. We apply their results at 1420 MHz to our H I data. Note that the values given by Gao et al. [38] are derived from the eight observations toward 3C 138 during December 2020 and March and April 2021, and that the GPPS data were taken in a much longer period from 2019 to a recent date. Therefore applying the T_a/T_b converting factor of Gao et al. [38] to all the GPPS spectral line data is not ideal but a necessary step. Fortunately our results can be further verified by the EBHIS data (see sect. 3.6).

3.3   RFI mitigation

The GPPS survey piggyback H I data are very occasionally affected by narrow- and wide-band radio frequency interference. The narrow-band RFI occasionally affects tens of channels (several km s^{-1} in the velocity space) of a spectrum, which we can mask manually and replace them by using a linear interpolation of their neighbours. The wide-band RFI extends several hundreds of km s^{-1}. It has to be fitted and removed together with the standing wave and baseline by the routine described in sect. 3.4 below.

3.4   Standing waves and baseline

The radio wave reflections between the main dish and the receiver cabin of a telescope cause periodic fluctuations in the spectra, which is known as the "standing waves". The standing wave frequency of FAST is about 1 MHz, corresponding to a velocity width of about 200 km s^{-1} for the H I line. The standing waves are one of the main nuisances of extra-galactic H I observations of FAST, but do not severely affect the observations of the Galactic H I signals, because the local H I signal is obviously stronger and wider. However, to obtain the accurate flux density and reveal the weak H I structures, standing waves must be removed.

A traditional method for removing the standing waves is to fit the line-free area of the spectrum by using a sine function, and then subtracting the fitted model from the data. However, we find that the standing waves of the GPPS H I spectrum vary with both time and frequency. A single sine function often fails in fitting the standing waves in the spectrum range wider than 1000 km s^{-1}.

A new routine which automatically fits the standing waves and the baseline together is developed in this work. The first step is to locate the H I line region in the frequency channels by calculating the rms of every 160 adjacent channels in the spectrum. The H I line region is identified with a threshold over 3σ level on this rms variation curve. The H I line identified through the rms data, instead of the original spectrum line, can avoid the mis-identification of the wide band RFI efficiently. An example is shown in Figure 2. The rms curve shown in the middle panel is calculated from the original spectrum in the top panel. The red line part marks the detected line region. This routine identifies the H I line accurately and ignores the wide band RFI in the velocity range of 200 to 500 km s^{-1}. The standing waves can then be fitted together with the baseline.

The second step is to apply the asymmetrically reweighted penalized least squares smoothing method (ArPLS [39,40]) to the line-free region. The ArPLS method provides fast and accurate estimates to the baseline of the H I spectra.
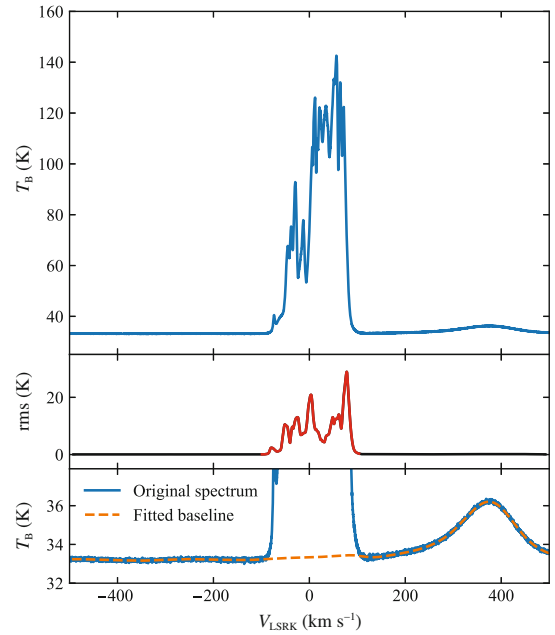
Figure 2   Example for the H I line finding and the baseline subtraction. Top panel is the original H I spectrum; middle panel shows the rms variation curve used to identify the H I line region, calculated from every 160 adjacent channels in the original H I spectrum shown in the top panel; bottom panel is the original spectrum (blue solid line) together with the fitted baseline and standing waves (orange dashed line) by the ArPLS [39, 40].

The fitting result stands for not only the standing waves but also other irrelevant features such as the continuum emission even in the range of the H I line, which is then subtracted from the original spectrum. Therefore the RFI, standing waves and the continuum emission have been all well removed. This approach works successfully on almost all spectra, only occasionally fails in a few cases because of strong RFI, for which we re-fit the baseline manually.

3.5   The stray radiation

The correction for the stray radiation of different beams has not yet been carried out for the current data set for this initial data release. Fortunately all the GPPS observations presented here are carried out by the main focus receiver with a zenith angle less than 26.4°, so that there is no spillover of the feed illumination beyond the edge of the 500-m primary reflector.

3.6   Calibrate the GPPS gain for the H I line to EBHIS

As described above in sect. 3.2, the GPPS survey has already accumulated data for a long period of time from 2019 to 2022. However, the conversion factor between T_a to T_b is derived from the observations toward 3C 138 in December 2020, and March and April in 2021. Therefore it does not work perfectly for all the survey data obtained in such a long
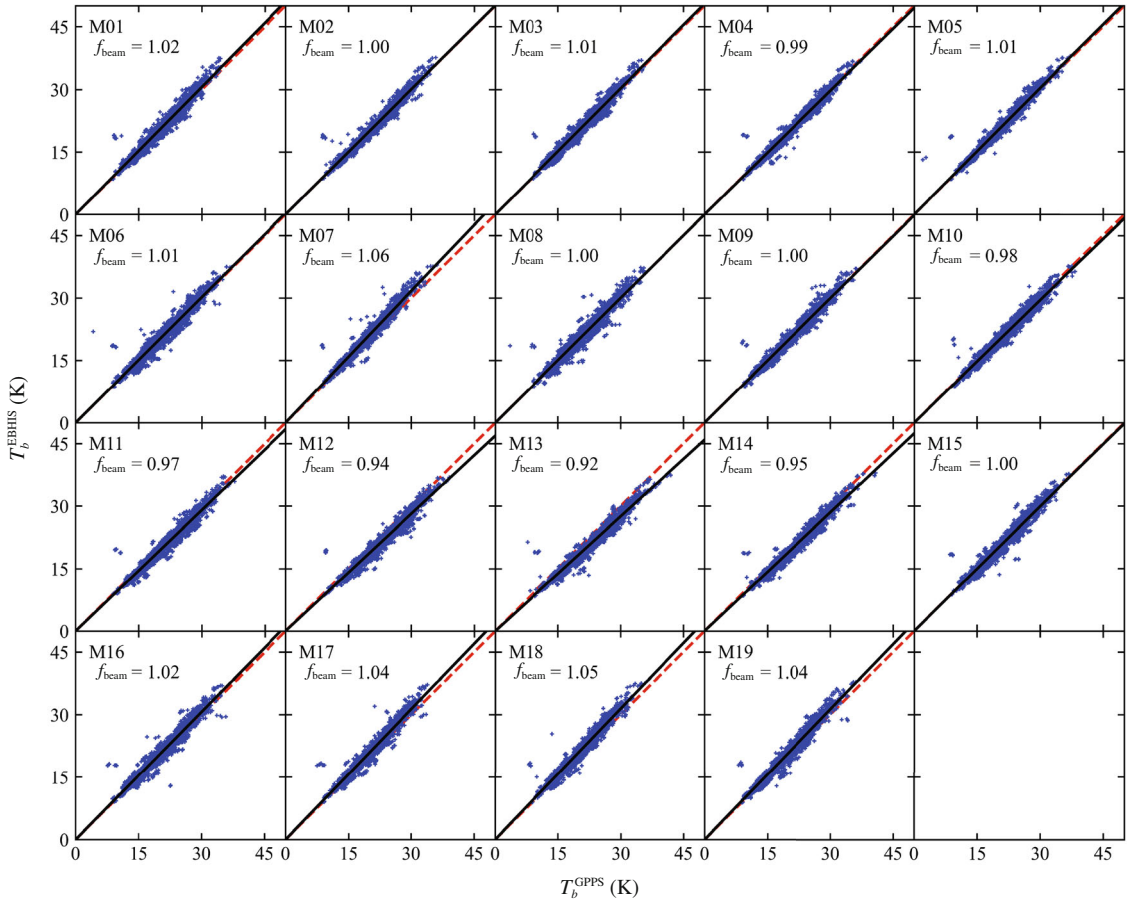
Figure 3 Comparison of the GPPS mean brightness temperatures with those data of the EBHIS for each of 19 beams (beam No. M01 to M19) respectively yield the gain correction factor f_{beam} for each beam. The solid lines present the best fitting relations to the data, the dashed lines stand for the equality.

time. The long-term gain variations of the 19-beam receiver have to be calibrated. We compare the GPPS H I data with the EBHIS data. The EBHIS survey was observed and well calibrated by a fully steerable single-dish telescope with a 7-beam receiver, hence provides a similar antenna status in all directions over the sky, though the EBHIS data has a coarser resolution.

The GPPS H I data are calibrated based on the EBHIS results in two steps. The first step is to scale the different gains of 19 beams. We first smooth the GPPS H I data cube to the same beam size of 10.8′ as the EBHIS, and then spilt all the data into 19 sub-data sets each corresponding to one FAST beam (i.e., M01 to M19). Comparison between the mean brightness temperature obtained by the GPPS survey and those from the EBHIS in the velocity range of −150 to 150 km s^{-1} for these sub-data sets gives a scaling factor from 0.92 to 1.06 for each beam, as shown by the best fitting slopes in Figure 3. These values are taken as the correction factors f_{beam} for each beam. After this step, the slightly different gains of the 19 beams near the 1420 MHz are well calibrated.

After gain corrections for different beams, some bright-

ness variations emerge between different snapshot covers. Similarly, we calibrate the gain variations of a given cover as a whole based on the comparison of the smoothed GPPS data with the EBHIS data. The calibration factors f_{cover} are in the range of 0.84 to 1.11, and the distribution of f_{cover} is shown in Figure 4.
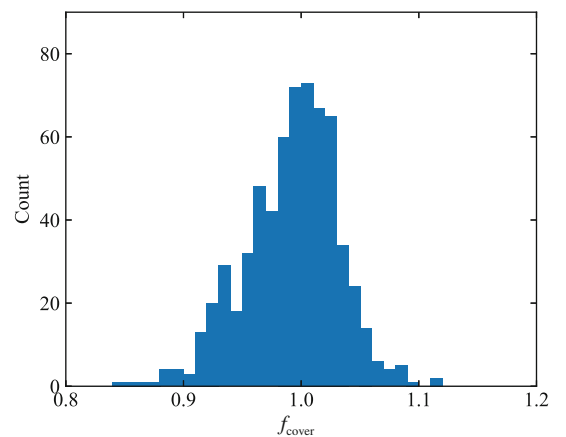

Figure 4 The number distribution of the cover gain calibration factor f_{cover}.

The calibration factors of f_{beam} and f_{cover} are applied together to the GPPS data to diminish the long time variation of the FAST gain, so that $T_b^{corrected} = T_b^{obs} \times f_{beam} \times f_{cover}$. The so-obtained GPPS brightness temperature is then very smooth and agrees with EBHIS data with a mean relative difference of only 1% (see sect. 4.2).

4   H I survey results

We process the piggyback spectral data of the GPPS survey [35] and obtain the first part of the Galactic H I spectra data in the region of $33° \leq l \leq 55°$ and $|b| \leq 2°$ in this work. The observations were conducted between March 2019 and October 2022 using the FAST L-band 19-beam receiving system. The results are also available on the webpage[2] for a data cube (l, b, v) of the Galactic plane. All spectra are Doppler-shifted to the kinematic local standard of rest (LSRK), the velocity range covered by the data cube

is -300 km s^{-1} $\leq V_{LSRK} \leq 300$ km s^{-1} with a raw velocity resolution of 0.1 km s^{-1} and a spatial resolution of 2.9′. In Figure 5, we show the image of the total H I column density integrated over the velocity range of -150 to 150 km s^{-1}, the range most of the Galactic H I structures have, by using the optically thin scaling factor of 1.823×10^{18} cm^{-2}/(K km s^{-1}) [1]. The map is gridded with $1' \times 1'$ pixels. Clearly seen in the map, the areas with low H I column densities correspond to relatively strong continuum emission sources, which often show absorption features on the H I spectra after the strong continuum emission even in the absorption line range is subtracted in the step of baseline fitting. More detailed channel maps in the velocity range of -80 to 120 km s^{-1} are presented in Figure 6 with a channel width of 20 km s^{-1}. The H I structures trace the large-scale mass distribution in the Milky Way, and the H I distribution in the velocity space roughly relates to the distances of the structures. In the H I images in the velocity range of -80 km s^{-1} $< V_{LSRK} < -20$ km s^{-1}, the
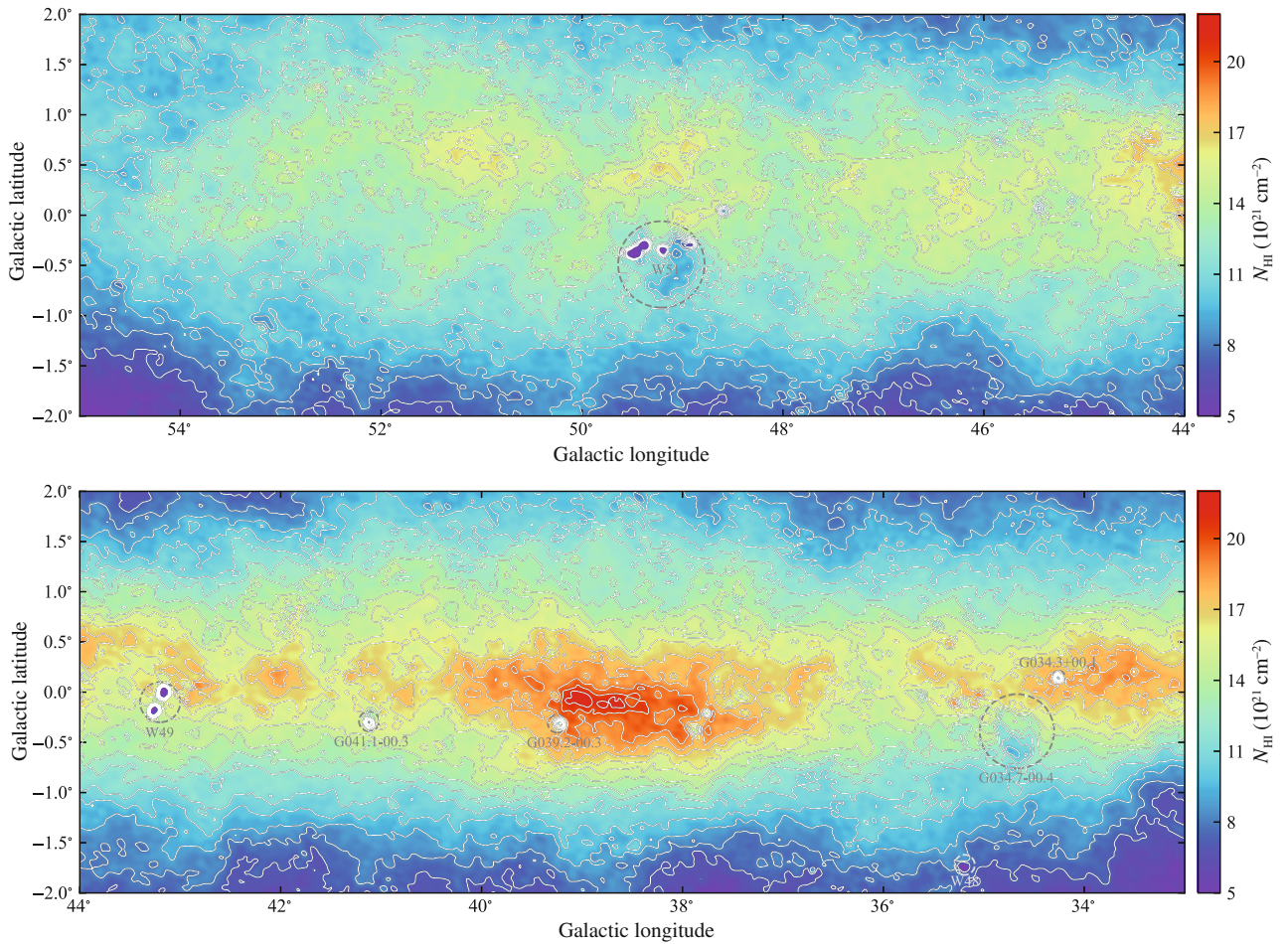
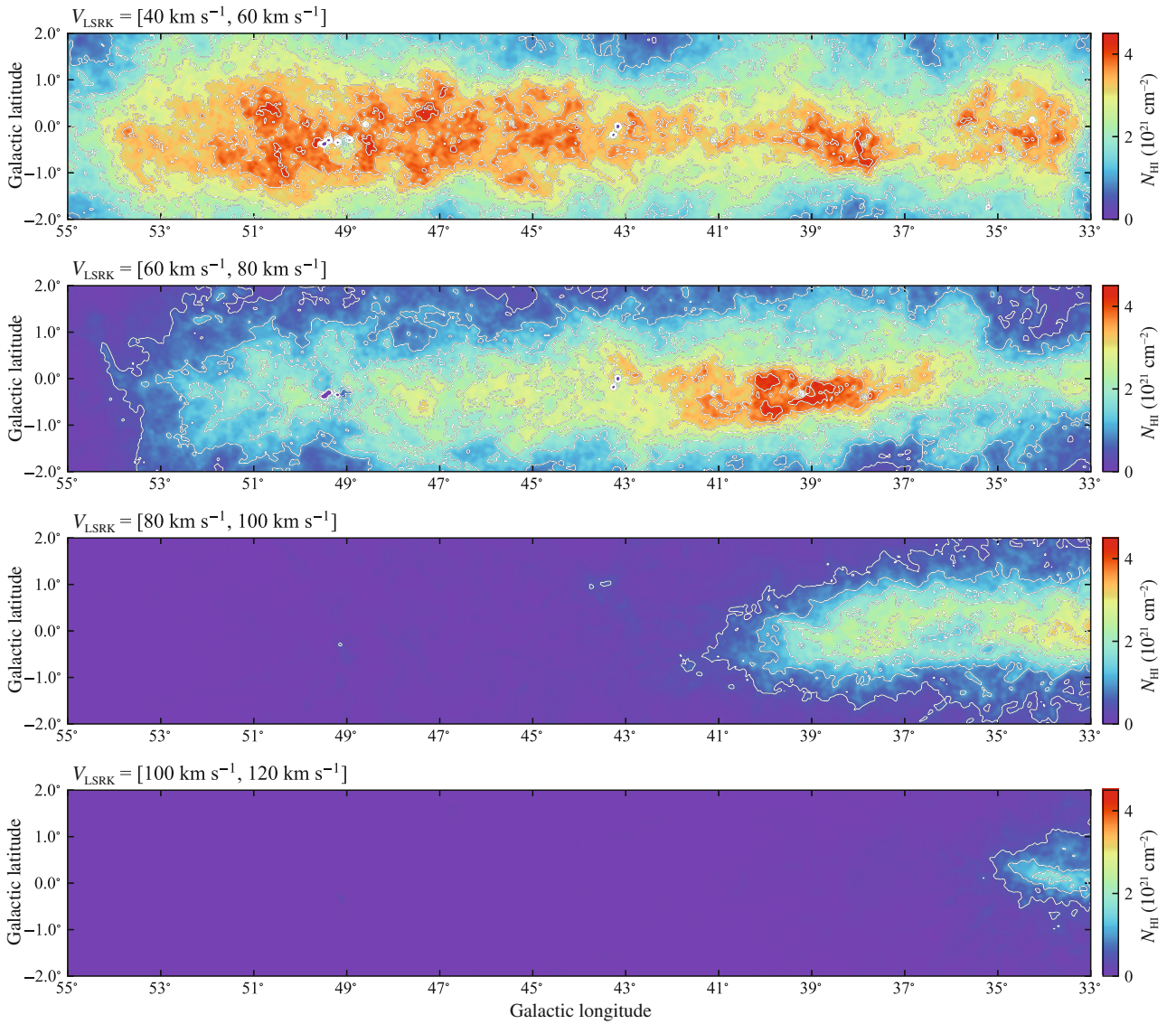
Figure 5   The H I column density map integrated over the velocity range of -150 to 150 km s^{-1}. The overlaid contour levels are 7 to 21×10^{21} cm^{-2} with a step of 1×10^{21} cm^{-2}. Low H I column density areas correspond to star formation complexes W48, W49 and W51, supernova remnants G034.7−00.4, G039.2−00.3 and G041.1−00.3, and H II region G034.3+00.1 as marked by dashed circles.
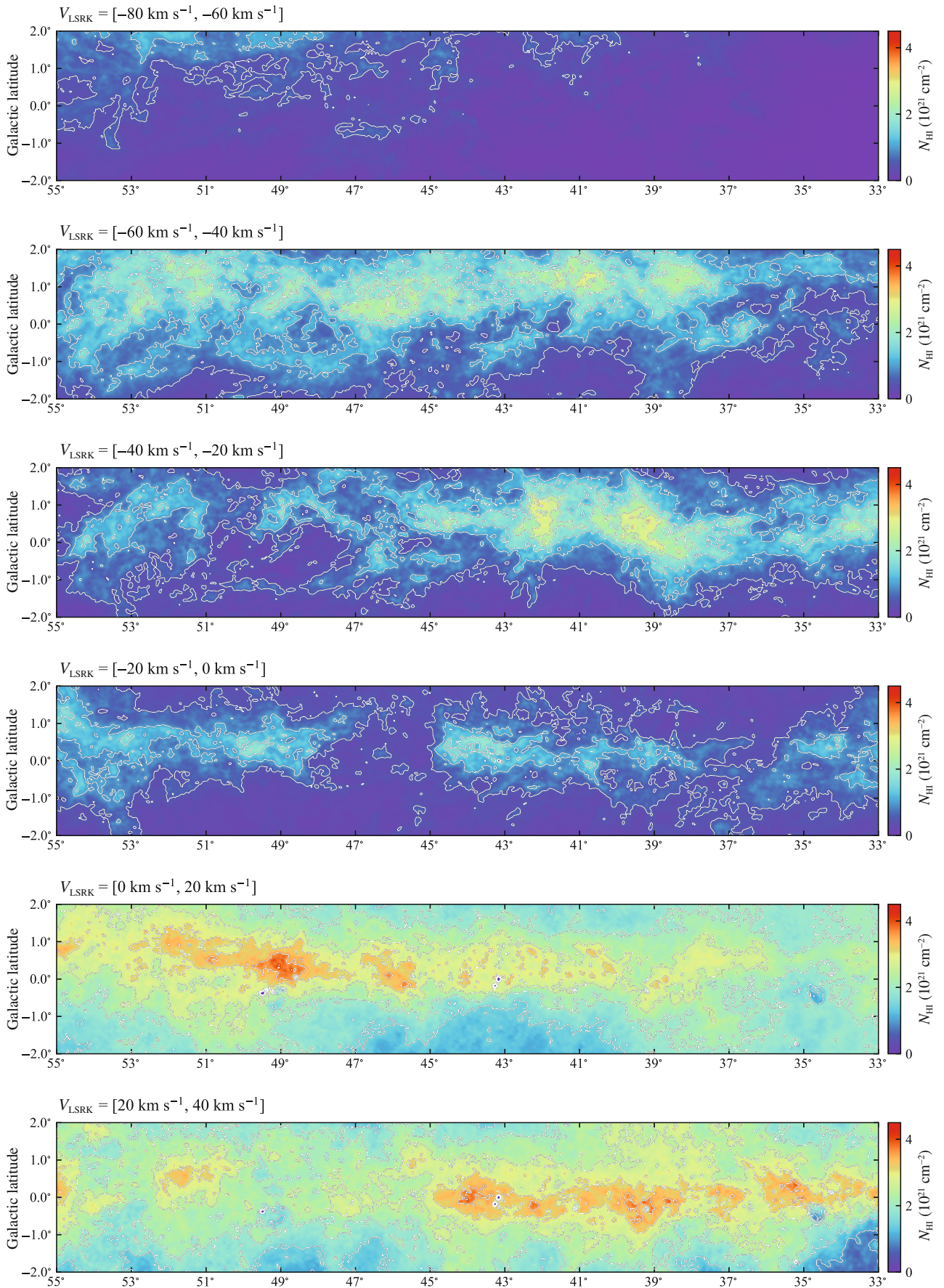
Figure 6 Channel maps of the H<small>I</small> column density in the velocity range of −80 to 120 km s^{-1} with a channel width of 20 km s^{-1}. The overlaid contour levels are 0.5 to 4 ×10^{21} cm^{-2} with a step of 0.5 ×10^{21} cm^{-2}.

bright H<small>I</small> emission structures are obviously offset to high Galactic latitudes, which indicates the warp of the outer Galactic disk [2].

4.1 Sensitivity assessment

The rms values of the spectra are calculated as the noise of 1000 H<small>I</small> line-free channels at a velocity resolution of 0.1 km s^{-1}(corresponding to the velocity range of −300 to −250 km s^{-1} and also the range of +250 to +300 km s^{-1}), and the rms map is shown in Figure 7. The distribution of rms values is shown in Figure 8. The median rms is 40.2 mK. After the tail of the large value end caused by the strong radio sources is excluded, the rms distribution can be fitted with a Gaussian peak at (39.9 ± 6.8) mK. Therefore

the value of 40 mK is adopted as the sensitivity of the piggyback H<small>I</small> observations in this section of the FAST GPPS survey.

As shown in Figure 7, the rms is generally uniform over the surveyed area, except for a few regions of strong continuum sources of star forming regions and supernova remnants. Besides the areas marked in Figure 5, high rms spots are noticed in Figure 7 for the supernova remnants: G033.6+00.1, and G046.8−00.3, and H<small>II</small> regions: G45.5+0.00, G45.5+00.1 and G048.6+00.0. The high rms structure centered at $l = 51.2°$, $b = 0.1°$ is a supernova remnant candidate reported by Anderson et al. [41]. We also notice a high rms area at $l = 37.0°$ to $38.0°$, $b = −0.4°$ to $0.0°$, not only one or two H<small>II</small> regions but about 20 H<small>II</small> regions are located in this region [42].
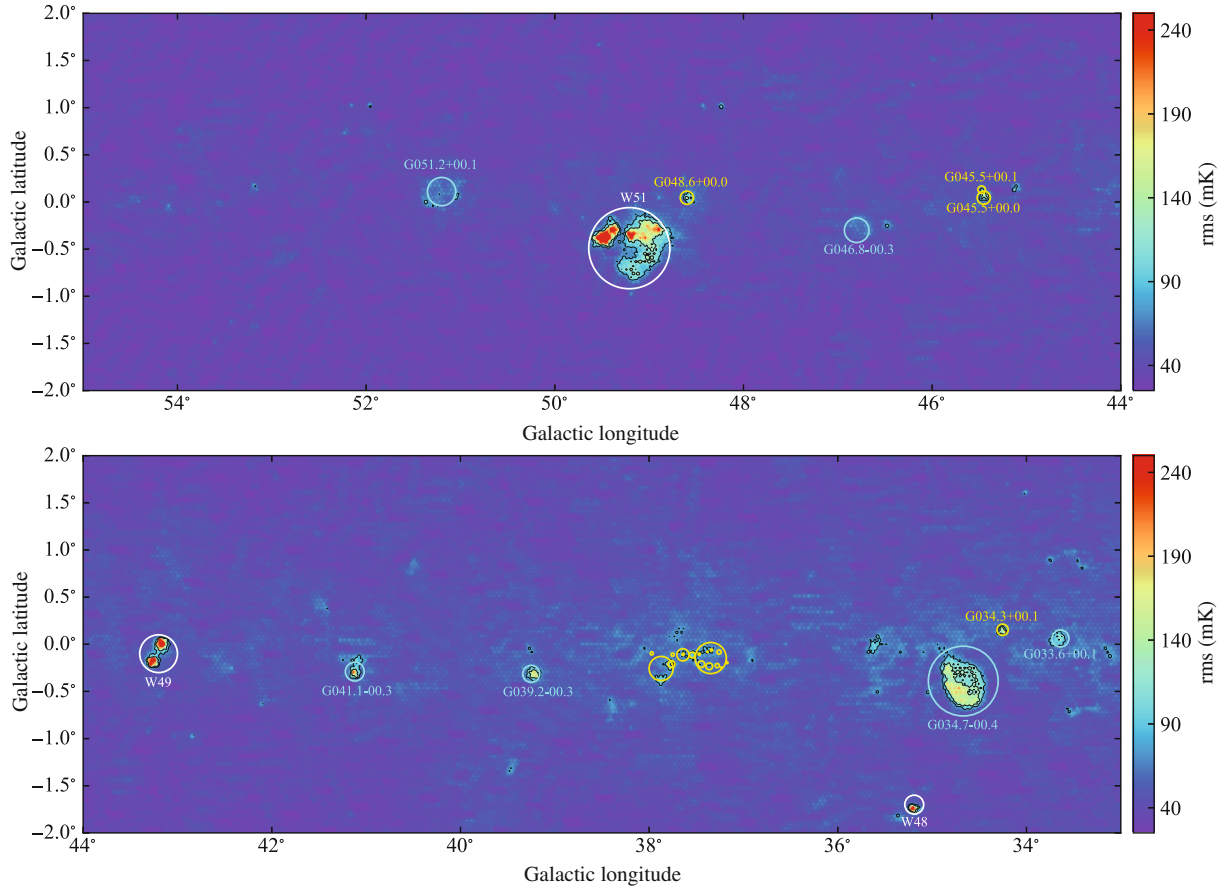
Figure 7   The rms map of the GPPS Galactic H I data cube with a spatial resolution of 2.9′ and a velocity resolution of 0.1 km s^{-1} in a grid of 1′ × 1′. The strong continuum emission sources cause relatively high rms, as indicated by circles: star formation complexes W48, W49 and W51 by white circles; supernova remnants G033.6+00.1, G034.7−00.4, G039.2−00.3, G041.1−00.3, G046.8−00.3 and supernova remnant candidate G051.2+00.1 by cyan circles; H II regions G034.3+00.1, G45.5+0.00, G45.5+00.1 and G048.6+00.0 by yellow circles, together the H II regions in the region of l = 37.0° to 38.0°, b = −0.4° to 0.0° without labels. The overlaid contour levels are 80 and 120 mK, corresponding to the double and triple of the rms value of 40 mK across the area (see Figure 8).

4.2   Comparison with EBHIS and GALFA-H I

We check the consistency of the GPPS H I column density integrated in the velocity range of −150 to 150 km s^{-1} with the EBHIS survey data. The GPPS data cube is smoothed to the same spatial resolution as that of the EBHIS data. The comparison between the two surveys in the upper panel of Figure 9 shows a great consistence, with only a very small number of outliers at the areas of strong radio continuum sources including star forming regions W49 and W51. Once these outliers are excluded, the two data sets can be linked with a linear fit as:

$$N_{\mathrm{H\,I}}^{\mathrm{GPPS}} = 1.01 \cdot N_{\mathrm{H\,I}}^{\mathrm{EBHIS}} - 0.11 \times 10^{21}\ \mathrm{cm}^{-2}. \tag{1}$$

Considering the mean value of the H I column densities $\langle N_{\mathrm{H\,I}}^{\mathrm{GPPS}} \rangle = 11.7 \times 10^{21}\ \mathrm{cm}^{-2}$, the zero point offset of 0.11 × 10^{21} cm^{-2} corresponds to a relative offset of only about 1%.
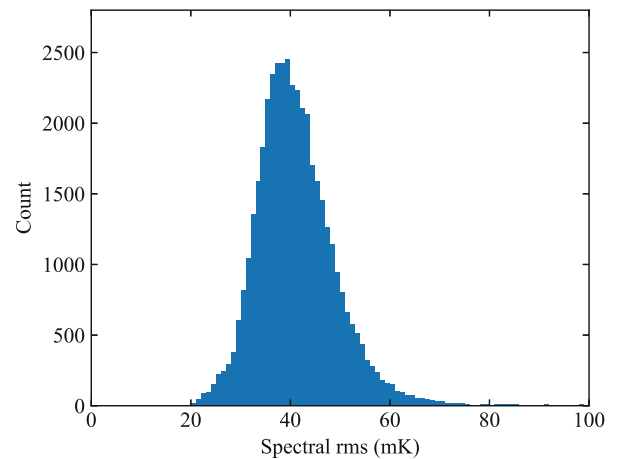
Figure 8   Number distribution of spectral rms values with a velocity resolution of 0.1 km s^{-1}. The tail end, which is induced by extremely bright continuum sources, contributes a very small fraction of the distribution and is excluded for legibility. The mean is 41.8 mK, and the median is 40.2 mK. After excluding the tail in the higher end induced by strong continuum sources, the distribution can be fitted with a Gaussian with a peak of (39.9±6.8) mK.

The same comparison is made with the GALFA-Hɪ data. We show it in the lower panel of Figure 9 and find

$$N_{\mathrm{Hi}}^{\mathrm{GPPS}} = 1.05 \cdot N_{\mathrm{Hi}}^{\mathrm{GALFA\text{-}Hi}} - 0.58 \times 10^{21} \ \mathrm{cm}^{-2}, \tag{2}$$

which indicates that the two data sets agree with each other within 5%.

4.3 Capability to detect exquisite Hɪ structures

The GPPS piggyback HI data have a high spatial resolution of 2.9′ and a great sensitivity, and therefore weak and exquisite Hɪ structures can be well detected. Here we show three examples in Figure 10 to demonstrate the quality of the GPPS Hɪ data. A huge amount of such structure details are left for readers to explore.
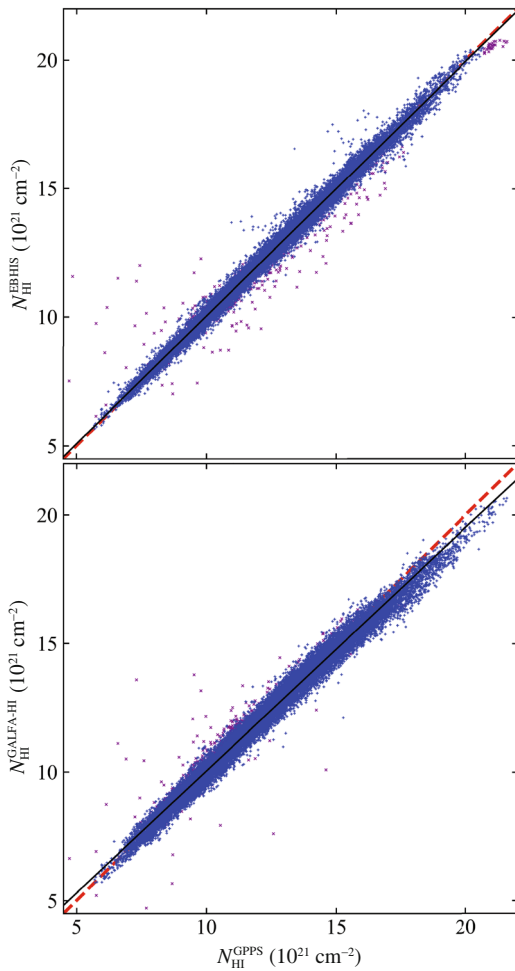
In the top panels of Figure 10, the very fine Hɪ spectra obtained from the GPPS survey data are presented for

Figure 9 Comparison of the total Hɪ column densities from the GPPS survey with the EBHIS data (upper panel) and GALFA-Hɪ (lower panel) shows a great consistence, with some outliers (shown as little purple "×") due to strong continuum sources. The red dashed line stands for equality, and the black solid line is a linear fitting to the data after excluding outliers.

three peaks in the areas around $(l, b) = (42.9°, 0.3°)$, $(l, b) = (44.0°, −0.5°)$ and $(l, b) = (50.4°, −0.6°)$, together with the spectra from the EBHIS. Careful comparison of the line wings demonstrates that the faint clouds are detected by the GPPS survey. To show these clouds, the column density images are presented in the panels in the second row of Figure 10, which are made by the integration over the velocity ranges indicated by the vertical lines in the inserted panels for the enlarged spectra. Clearly the exquisite Hɪ structures are shown in unprecedented details, not only with elongated structures but also some compact cloud cores.
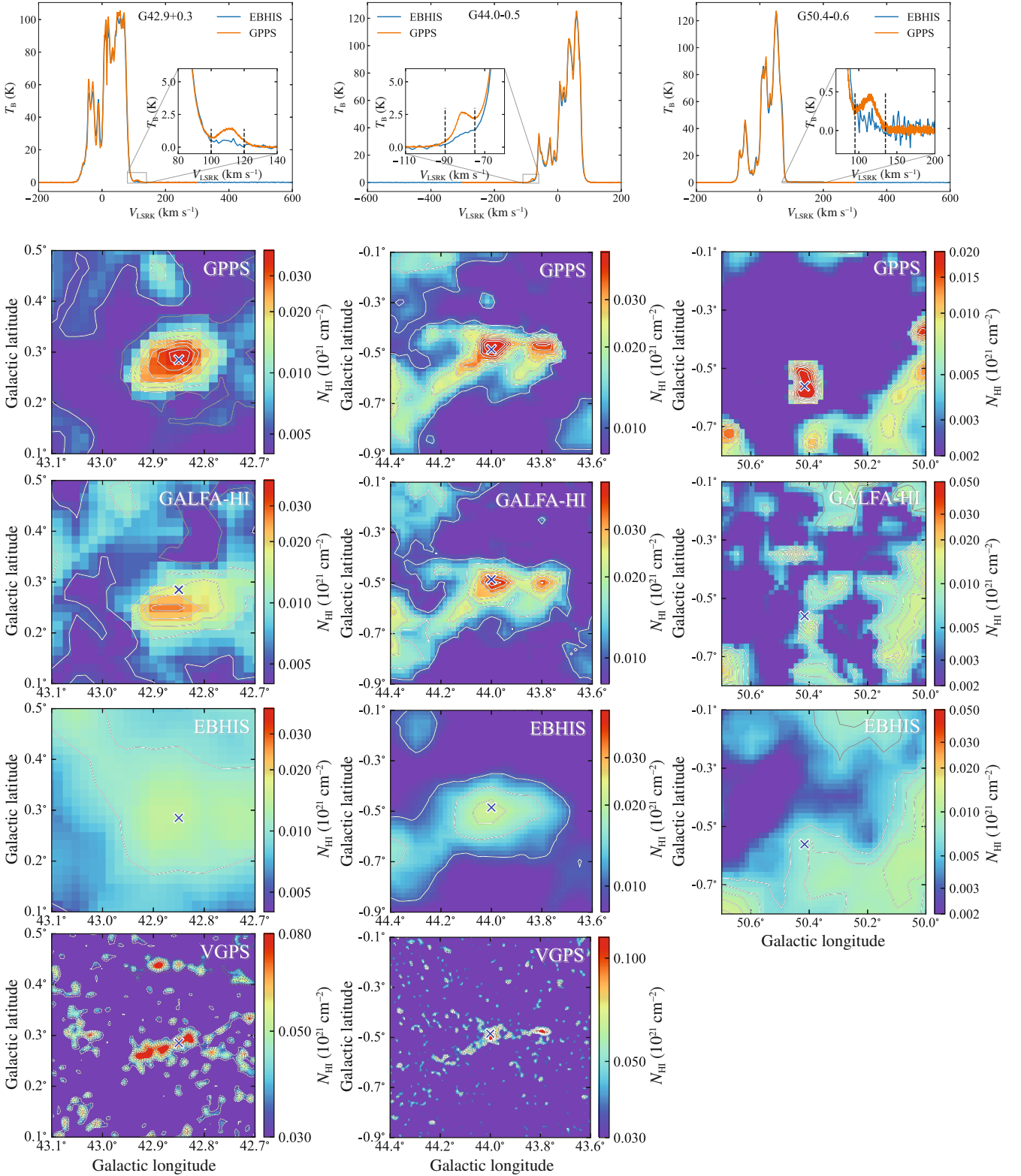
To verify if these structures are real, we extract the Hɪ data from the EBHIS [10], GALFA-Hɪ [13] and VGPS [4] for comparisons. The column density images are obtained by integrating in the same velocity ranges, and they are shown in the panels of the third, fourth and bottom rows of Figure 10. For all three regions, the EBHIS Hɪ maps [10] confirm bright structures or cloud cores in a smoothed style due to its larger beam size. The GALFA-Hɪ maps have a spatial resolution of 4′, it resolves the three structures better than the EBHIS data, and again confirm the FAST GPPS detection. In the high resolution Hɪ column density maps from the VGPS [4], the compact cloud cores are detected for the regions of $(l, b) = (42.9°, 0.3°)$ and $(l, b) = (44.0°, −0.5°)$, and the map for the region of $(l, b) = (50.4°, −0.6°)$ is severely affected by the RFI. The maps from the EBHIS, GALFA-Hɪ and VGPS therefore confirm that the detection of both extended structures and compact cloud cores by the FAST GPPS Hɪ data are reliable. The FAST GPPS Hɪ data have a better resolution and a better sensitivity than GALFA-Hɪ (see Table 1).

Using the kinematic model of the Milky Way developed by Reid et al. [43], the distances of these three exquisite Hɪ clouds can be estimated. The kinematic distances of Hɪ clouds may have a large uncertainty, and also suffer from the near and far side ambiguity inside the solar circle. The Hɪ cloud at $(l, b) = (44.0°, −0.5°)$ in the middle column of Figure 10 is located at an extreme negative velocity of $V_{\mathrm{LSRK}} \sim −81$ km s^{-1}, we estimate the kinematic distance of this Hɪ cloud as being approximately 21.1 kpc. The clouds at $(l, b) = (42.9°, 0.3°)$ and $(l, b) = (50.4°, −0.6°)$ have large positive velocities of $V_{\mathrm{LSRK}} \sim 110$ and 114 km s^{-1}, much larger than the possible velocities at the tangents of 73.4 and 53.8 km s^{-1}, respectively. The peculiar velocities of the cloud cores must be larger than 36.6 and 60.2 km s^{-1}, respectively.

In the region around $(l, b) = (50.4°, −0.6°)$, the GPPS Hɪ spectrum of the Hɪ image peak shows a clear bump in the velocity range of 100 to 135 km s^{-1} with a peak brightness temperature of only 0.18 K, which is buried in the noise on the EBHIS spectrum. This GPPS integrated Hɪ image probably presents one of the weakest exquisite Hɪ structures in our Milky Way so far.

Figure 10   Three examples of weak exquisite H I structures detected in the piggyback H I data of the GPPS survey. The H I spectra from the image peaks marked by "×" in the panels of the second row are shown in the top panels by the orange lines together with the EBHIS spectra [10] in blue lines, and the integrated column density images are shown in the second row of panels. The velocity range for the integrated images is indicated by the vertical dashed lines in the inserted enlarged plots of the top panels. For comparison, the integrated column density images from the GALFA-H I [13], EBHIS [10] and the VGPS [4] are shown in the panels of the third, fourth and the bottom rows, respectively. The exquisite H I structures in the right panels are detected only in the GPPS survey, and it is too weak to be detected by the EBHIS (see the spectrum in the top panel) or the GALFA-H I. The VGPS data are polluted by RFI (image not shown).
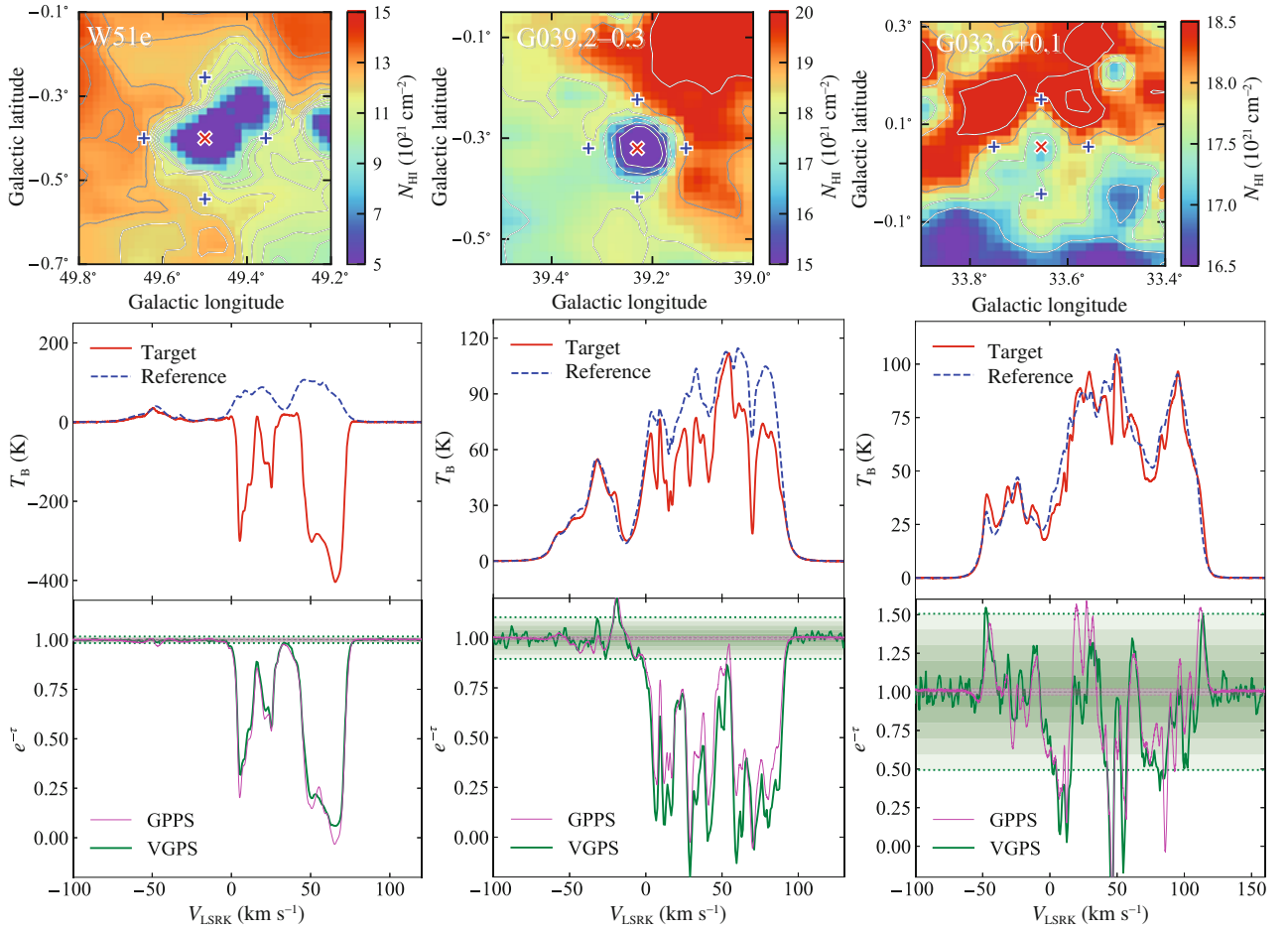
Figure 11   The Hɪ absorption features observed against W51e (left panels), SNR G039.2–0.3 (middle panels) and SNR G033.6+0.1 (right panels), respectively. The top panels show the integrated Hɪ column density map over the velocity range of −150 to 150 km s^{-1} centered at the targeted radio sources marked by the red "×". The middle panels show the GPPS Hɪ spectra at the "target" (red solid line) and the averaged spectra from the four "reference" positions marked by "+" in the top map. The bottom panels show the Hɪ absorption spectra $e^{-\tau}$ extracted from GPPS Hɪ data (magenta solid line), together with those from the VGPS data (green solid line, ref. [4]), here τ is the optical depth. The shadow area and the magenta and green dotted lines indicate ±5σ area for the GPPS and VGPS spectrum, here the rms σ is calculated from the line-free range of the spectra.

4.4 Hɪ absorption features

The most significant low column density spots in Figure 5 are the star formation complexes: W49 and W51; the supernova remnants: G034.7–00.4, G039.2–00.3 and G041.1–00.3, and the strong Hɪɪ region G034.3+00.1. When observing the Hɪ against bright continuum sources, absorption is produced by neutral medium [44]. Continuum emission was subtracted in our data processing by the ArPLS [39, 40] as the baseline in data. Comparing with observations by using interferometers which can filter the unrelated surrounding diffuse emission, the results of single dish observations contain the emission and absorption of the source and also the emission of surrounding gas. Nevertheless, the high sensitivity of the GPPS Hɪ data still provides a great chance for Hɪ absorption line studies. In Figure 11, we show three examples for the Hɪ absorption lines, one star-formation region and two SNRs.

The Hɪ absorption lines of other sources can be extracted by readers for their interests.

W51 is one of the most active star-forming complexes in the Milky Way. It appears to be the lowest Hɪ column density region in Figure 5. We extract the Hɪ absorption spectrum of W51e by selecting the center of the region as the target point (red cross in the top left panel of Figure 11), the reference spectrum is the averaged spectrum from four points close to the target point but without strong continuum emission (blue crosses in the top left panel of Figure 11). By comparing the "target" and "reference" spectra, we obtain the Hɪ absorption spectrum $e^{-\tau}$ as shown in the bottom left panel (magenta solid line), together with the Hɪ absorption spectrum extracted from the VGPS data (green solid line) using the same target and reference positions. The magenta and green dotted lines and shadows indicate the ±5σ area of two spectra, respectively. As one of the strongest continuum sources,

almost the same absorption features are detected in the GPPS and VGPS Hɪ data in the positive velocity range. Because of the high sensitivity and velocity resolution, GPPS-Hɪ data reveal some sharper absorption features, e.g., at the velocity of $V_{\text{LSRK}} \sim -46.5$ km s^{-1}.

SNR G039.2–0.3 (3C 396) is a young SNR, appearing as a low density spot on the bright Hɪ emission region in Figure 5 and the top middle panel of Figure 11. The Hɪ absorption spectra from the GPPS survey (this paper) and the VGPS data [4] are shown in the middle column of Figure 11. The rms of the GPPS spectrum is about 25 times smaller than that of VGPS data. In general, in the velocity range of $V_{\text{LSRK}} = -10$ to 90 km s^{-1} the main absorption features of the two spectra are very similar, and the VGPS spectrum shows deeper absorption. The difference of absorption lines mainly comes from the different beam size of the two surveys, since a large telescope beam should have a beam smearing effect and hence weakens the absorption signal [44]. Another source of the difference is the filtering effect of interferometers. The GPPS Hɪ data contain the emission from large scale Hɪ structures but the VGPS does not.

G033.6+0.1 is also an SNR. The absorption is obvious in the integrated Hɪ map in Figure 5 and the top right panel of Figure 11, though it is among the faint continuum sources. We obtain the Hɪ absorption spectra and show it in the right column of Figure 11. The GPPS spectrum not only confirms the major VGPS absorption features, but also presents features at $V_{\text{LSRK}} \sim 8, 12, 47, 55, 75, 83, 85$ and 100 km s^{-1} with a good confidence because of the high sensitivity.

5   Summary

The piggyback spectral data simultaneously recorded in the FAST GPPS survey [35] are valuable resources for the Galactic Hɪ studies. It has an angular resolution of 2.9′. With the five minutes integration time of each FAST pointing, the rms of the brightness temperature noise of the GPPS Hɪ data is approximately 40 mK at a velocity resolution of 0.1 km s^{-1}, which is the most sensitive survey of Galactic Hɪ emission by far.

We process the GPPS Hɪ data. A new routine is developed for automatically fitting and removing the baseline and standing waves efficiently. The Hɪ line intensity is scaled by using the standard on-off calibration signals in each session. The comparison of the GPPS integrated Hɪ intensity maps with the EBHIS survey gives the beam calibration factors for 19 beams and the cover correction factors for each cover, so that the long-term gain variations can be relatively calibrated. Because of the special observation mode of the GPPS survey, the released GPPS Hɪ data cube is not Nyquist-sampled in

terms of the beam size. The correction for the stray radiation of different beams has not yet been carried out for the data set for this initial data release.

This first released GPPS Hɪ data are made for the survey area of $33° \leq l \leq 55°$ and $|b| \leq 2°$, with a velocity resolution of 0.1 km s^{-1} in the velocity range of -300 km s$^{-1} \leq V_{\text{LSRK}} \leq 300$ km s^{-1}, which can be used to detect exquisite interstellar Hɪ structures and improve our understanding of the interstellar medium.

Data availability

Original FAST GPPS survey data, including the piggyback spectral line data, will be released one year after observations, according to the FAST data release policy. All processed Hɪ data as presented in this paper is available on the project web-page: http://zmtt.bao.ac.cn/MilkyWayFAST/.

1   S. R. Kulkarni, and C. Heiles, *Interstellar Processes*, edited by D. J. Hollenbach, J. Thronson, and A. Harley, Vol. 134 (Astrophysics and Space Science Library, Dordrecht, 2007), p. 87.

2   P. M. W. Kalberla, and J. Kerp, Annu. Rev. Astron. Astrophys. **47**, 27 (2009).

3   R. S. Klessen, and S. C. O. Glover, Saas-Fee Advanced Course **43**, 85 (2016).

4   J. M. Stil, A. R. Taylor, J. M. Dickey, D. W. Kavars, P. G. Martin, T. A. Rothwell, A. I. Boothroyd, F. J. Lockman, and N. M. McClure-Griffiths, Astron. J. **132**, 1158 (2006), arXiv: astro-ph/0605422.

5   J. M. Dickey, N. McClure-Griffiths, S. J. Gibson, J. F. Gòmez, H. Imai, P. Jones, S. Stanimirović, J. T. Van Loon, A. Walsh, A. Alberdi, G. Anglada, L. Uscanga, H. Arce, M. Bailey, A. Begum, B. Wakker, N. B. Bekhti, P. Kalberla, B. Winkel, K. Bekki, B. Q. For, L. Staveley-Smith, T. Westmeier, M. Burton, M. Cunningham, J. Dawson, S. Ellingsen, P. Diamond, J. A. Green, A. S. Hill, B. Koribalski, D. McConnell, J. Rathborne, M. Voronkov, K. A. Douglas, J. English, H. A. Ford, F. J. Lockman, T. Foster, Y. Gomez, A. Green, J. Bland-Hawthorn, S. Gulyaev, M. Hoare, G. Joncas, J. H. Kang, C. R. Kerton, B. C. Koo, D. Leahy, N. Lo, V. Migenes, J. Nakashima, Y. Zhang, D. Nidever, J. E.

G. Peek, D. Tafoya, W. Tian, and D. Wu, Publ. Astron. Soc. Aust. **30**, e003 (2013), arXiv: 1207.0891.

6 A. R. Taylor, S. J. Gibson, M. Peracaula, P. G. Martin, T. L. Landecker, C. M. Brunt, P. E. Dewdney, S. M. Dougherty, A. D. Gray, L. A. Higgs, C. R. Kerton, L. B. G. Knee, R. Kothes, C. R. Purton, B. Uyaniker, B. J. Wallace, A. G. Willis, and D. Durand, Astron. J. **125**, 3145 (2003).

7 N. M. McClure-Griffiths, J. M. Dickey, B. M. Gaensler, A. J. Green, M. Haverkorn, and S. Strasser, Astrophys. J. Suppl. S. **158**, 178 (2005), arXiv: astro-ph/0503134.

8 Y. Wang, H. Beuther, M. R. Rugel, J. D. Soler, J. M. Stil, J. Ott, S. Bihr, N. M. McClure-Griffiths, L. D. Anderson, R. S. Klessen, P. F. Goldsmith, N. Roy, S. C. O. Glover, J. S. Urquhart, M. Heyer, H. Linz, R. J. Smith, F. Bigiel, J. Dempsey, and T. Henning, Astron. Astrophys. **634**, A83 (2020), arXiv: 1912.08223.

9 P. M. W. Kalberla, W. B. Burton, D. Hartmann, E. M. Arnal, E. Bajaja, R. Morras, and W. G. L. Pöppel, Astron. Astrophys. **440**, 775 (2005).

10 B. Winkel, J. Kerp, L. Flöer, P. M. W. Kalberla, N. Ben Bekhti, R. Keller, and D. Lenz, Astron. Astrophys. **585**, A41 (2016), arXiv: 1512.05348.

11 P. M. W. Kalberla, N. M. McClure-Griffiths, D. J. Pisano, M. R. Calabretta, H. Alyson Ford, F. J. Lockman, L. Staveley-Smith, J. Kerp, B. Winkel, T. Murphy, and K. Newton-McGee, Astron. Astrophys. **521**, A17 (2010), arXiv: 1007.0686.

12 N. Ben Bekhti, L. Flöer, R. Keller, J. Kerp, D. Lenz, B. Winkel, J. Bailin, M. R. Calabretta, L. Dedes, H. A. Ford, B. K. Gibson, U. Haud, S. Janowiecki, P. M. W. Kalberla, F. J. Lockman, N. M. McClure-Griffiths, T. Murphy, H. Nakanishi, D. J. Pisano, and L. Staveley-Smith, Astron. Astrophys. **594**, A116 (2016), arXiv: 1610.06175.

13 J. E. G. Peek, B. L. Babler, Y. Zheng, S. E. Clark, K. A. Douglas, E. J. Korpela, M. E. Putman, S. Stanimirović, S. J. Gibson, and C. Heiles, Astrophys. J. Suppl. Ser. **234**, 2 (2018).

14 N. M. Pingel, J. Dempsey, N. M. McClure-Griffiths, J. M. Dickey, K. E. Jameson, H. Arce, G. Anglada, J. Bland-Hawthorn, S. L. Breen, F. Buckland-Willis, S. E. Clark, J. R. Dawson, H. Dénes, E. M. Di Teodoro, B. Q. For, T. J. Foster, J. F. Gómez, H. Imai, G. Joncas, C. G. Kim, M. Y. Lee, C. Lynn, D. Leahy, Y. K. Ma, A. Marchal, D. McConnell, M. A. Miville-Deschênes, V. A. Moss, C. E. Murray, D. Nidever, J. Peek, S. Stanimirović, L. Staveley-Smith, T. Tepper-Garcia, C. D. Tremblay, L. Uscanga, J. T. van Loon, E. Vázquez-Semadeni, J. R. Allison, C. S. Anderson, L. Ball, M. Bell, D. C. J. Bock, J. Bunton, F. R. Cooray, T. Cornwell, B. S. Koribalski, N. Gupta, D. B. Hayman, L. Harvey-Smith, K. Lee-Waddell, A. Ng, C. J. Phillips, M. Voronkov, T. Westmeier, and M. T. Whiting, Publ. Astron. Soc. Aust. **39**, e005 (2022), arXiv: 2111.05339.

15 J. M. Dickey, J. M. Dempsey, N. M. Pingel, N. M. McClure-Griffiths, K. Jameson, J. R. Dawson, H. Dénes, S. E. Clark, G. Joncas, D. Leahy, M. Y. Lee, M. A. Miville-Deschenes, S. Stanimirović, C. D. Tremblay, and J. T. van Loon, Astrophys. J. **926**, 186 (2022), arXiv: 2111.04545.

16 N. M. McClure-Griffiths, D. J. Pisano, M. R. Calabretta, H. A. Ford, F. J. Lockman, L. Staveley-Smith, P. M. W. Kalberla, J. Bailin, L. Dedes, S. Janowiecki, B. K. Gibson, T. Murphy, H. Nakanishi, and K. Newton-McGee, Astrophys. J. Suppl. Ser. **181**, 398 (2009), arXiv: 0901.1159.

17 P. M. W. Kalberla, and U. Haud, Astron. Astrophys. **578**, A78 (2015), arXiv: 1505.01011.

18 J. E. G. Peek, C. Heiles, K. A. Douglas, M. Y. Lee, J. Grcevich, S. Stanimirović, M. E. Putman, E. J. Korpela, S. J. Gibson, A. Begum, D. Saul, T. Robishaw, and M. Krčo, Astrophys. J. Suppl. Ser. **194**, 20 (2011), arXiv: 1101.1879.

19 W. B. Burton, Astron. Astrophys. **10**, 76 (1971).

20 E. S. Levine, L. Blitz, and C. Heiles, Science **312**, 1773 (2006), arXiv: astro-ph/0605728.

21 B. C. Koo, G. Park, W. T. Kim, M. G. Lee, D. S. Balser, and T. V. Wenger, Publ. Astron. Soc. Pacific **129**, 094102 (2017), arXiv: 1706.10084.

22 P. M. W. Kalberla, J. Kerp, U. Haud, B. Winkel, N. B. Bekhti, L. Flöer, and D. Lenz, Astrophys. J. **821**, 117 (2016), arXiv: 1602.07604.

23 J. D. Soler, H. Beuther, J. Syed, Y. Wang, L. D. Anderson, S. C. O. Glover, P. Hennebelle, M. Heyer, T. Henning, A. F. Izquierdo, R. S. Klessen, H. Linz, N. M. McClure-Griffiths, J. Ott, S. E. Ragan, M. Rugel, N. Schneider, R. J. Smith, M. C. Sormani, J. M. Stil, R. Treß, and J. S. Urquhart, Astron. Astrophys. **642**, A163 (2020), arXiv: 2007.07285.

24 J. D. Soler, M. A. Miville-Deschnes, S. Molinari, R. S. Klessen, P. Hennebelle, L. Testi, N. M. McClure-Griffiths, H. Beuther, D. Elia, E. Schisano, A. Traficante, P. Girichidis, S. C. O. Glover, R. J. Smith, M. Sormani, and R. Treß, Astron. Astrophys. **662**, A96 (2022), arXiv: 2205.10426.

25 C. Li, K. Qiu, B. Hu, and Y. Cao, Astrophys. J. Lett. **918**, L2 (2021), arXiv: 2108.01905.

26 W. W. Tian, and D. A. Leahy, Mon. Not. R. Astron. Soc. **391**, L54 (2008).

27 S. Ranasinghe, and D. A. Leahy, Astron. J. **155**, 204 (2018), arXiv: 1808.09082.

28 S. J. Gibson, A. R. Taylor, L. A. Higgs, and P. E. Dewdney, Astrophys. J. **540**, 851 (2000).

29 S. J. Gibson, A. R. Taylor, L. A. Higgs, C. M. Brunt, and P. E. Dewdney, Astrophys. J. **626**, 195 (2005), arXiv: astro-ph/0503117.

30 D. Li, and P. F. Goldsmith, Astrophys. J. **585**, 823 (2003), arXiv: astro-ph/0206396.

31 N. Y. Tang, P. Zuo, D. Li, L. Qian, T. Liu, Y. F. Wu, M. Krčo, M. T. Liu, Y. L. Yue, Y. Zhu, H. F. Liu, D. J. Yu, J. H. Sun, P. Jiang, G. F. Pan, H. Li, H. Q. Gan, R. Yao, and S. Liu, Res. Astron. Astrophys. **20**, 077 (2020), arXiv: 1912.00588.

32 X. Liu, Y. Wu, C. Zhang, N. Tang, T. Liu, K. Wang, D. Li, L. Qian, S. L. Qin, J. Esimbek, J. Wang, J. Yuan, F. Xu, and L. Yuan, Astron. Astrophys. **658**, A140 (2022), arXiv: 2112.13717.

33 R. Nan, D. Li, C. Jin, Q. Wang, L. Zhu, W. Zhu, H. Zhang, Y. Yue, and L. Qian, Int. J. Mod. Phys. D **20**, 989 (2011), arXiv: 1105.3794.

34 P. Jiang, N. Y. Tang, L. G. Hou, M. T. Liu, M. Krčo, L. Qian, J. H. Sun, T. C. Ching, B. Liu, Y. Duan, Y. L. Yue, H. Q. Gan, R. Yao, H. Li, G. F. Pan, D. J. Yu, H. F. Liu, D. Li, B. Peng, and J. Yan, Res. Astron. Astrophys. **20**, 064 (2020), arXiv: 2002.01786.

35 J. L. Han, C. Wang, P. F. Wang, T. Wang, D. J. Zhou, J. H. Sun, Y. Yan, W. Q. Su, W. C. Jing, X. Chen, X. Y. Gao, L. G. Hou, J. Xu, K. J. Lee, N. Wang, P. Jiang, R. X. Xu, J. Yan, H. Q. Gan, X. Guan, W. J. Huang, J. C. Jiang, H. Li, Y. P. Men, C. Sun, B. J. Wang, H. G. Wang, S. Q. Wang, J. T. Xie, H. Xu, R. Yao, X. P. You, D. J. Yu, J. P. Yuan, R. Yuen, C. F. Zhang, and Y. Zhu, Res. Astron. Astrophys. **21**, 107 (2021), arXiv: 2105.08460.

36 L. G. Hou, J. L. Han, T. Hong, X. Y. Gao, and C. Wang, Sci. China-Phys. Mech. Astron. **65**, 129703 (2022), arXiv: 2211.11301.

37 J. Xu, J. L. Han, P. F. Wang, and Y. Yan, Sci. China-Phys. Mech. Astron. **65**, 129704 (2022), arXiv: 2211.11302.

38 X. Y. Gao, W. Reich, X. H. Sun, H. Zhao, T. Hong, Z. S. Yuan, P. Reich, and J. L. Han, Sci. China-Phys. Mech. Astron. **65**, 129705 (2022), arXiv: 2211.11408.

39 S. J. Baek, A. Park, Y. J. Ahn, and J. Choo, Analyst **140**, 250 (2015).

40 Q. Zeng, X. Chen, X. Li, J. L. Han, C. Wang, D. J. Zhou, and T. Wang, Mon. Not. R. Astron. Soc. **500**, 2969 (2021).

41 L. D. Anderson, Y. Wang, S. Bihr, M. Rugel, H. Beuther, F. Bigiel, E. Churchwell, S. C. O. Glover, A. A. Goodman, T. Henning, M. Heyer, R. S. Klessen, H. Linz, S. N. Longmore, K. M. Menten, J. Ott, N. Roy, J. D. Soler, J. M. Stil, and J. S. Urquhart, Astron. Astrophys. **605**, A58 (2017).

42 L. D. Anderson, T. M. Bania, D. S. Balser, V. Cunningham, T. V. Wenger, B. M. Johnstone, and W. P. Armentrout, Astrophys. J. Suppl. Ser. **212**, 1 (2014).

43 M. J. Reid, K. M. Menten, A. Brunthaler, X. W. Zheng, T. M. Dame, Y. Xu, Y. Wu, B. Zhang, A. Sanna, M. Sato, K. Hachisuka, Y. K. Choi, K. Immer, L. Moscadelli, K. L. J. Rygl, and A. Bartkiewicz, Astrophys. J. **783**, 130 (2014), arXiv: 1401.5377.

44 J. M. Dickey, and F. J. Lockman, Annu. Rev. Astron. Astrophys. **28**, 215 (1990).